university of groningen / faculty of science and engineering / biomedical engineering

Development of diffusion tensor imaging phantom for skeletal muscle characterization

Andrei Bogdan Ioanitescu

S4712560

Cognitive Neuroscience Center

Period 15/04/2024 - 08/07/2024

1^{st} Examiner: [Remco Renken, MR physicist, Cognitive Neuroscience Department]

2^{nd} Examiner: [Prashant Sharma, Associate Professor, Biomedical Engineering Department]

Abstract

Diffusion tensor imaging (DTI) represents a non-invasive imaging technique sensitive to microscopic diffusion, allowing quantification of the behaviour of water diffusion within human tissue. This tool contributes to the meaningful characterization of the skeletal muscle architecture and arrangement, which are important determinants of the muscle's functional features. However, due to the inconsistent character of the DTI quantification, there is a need for phantom validation of DTI analysis techniques. Therefore, this study aims to develop a DTI phantom that would serve as a muscle diffusion model, focussing to replicate the diffusion attributes found in skeletal muscle. Stereolithography (SLA) 3D printing technique was employed to create a structure containing multiple layers of curved strands, resembling the fibrous environment found in skeletal muscle. To account for the extracellular matrix between the muscle fibers, agar hydrogel of three different concentrations was introduced within the structure of the phantom. The phantom was scanned and compared with a healthy volunteer's DTI measurement of the rectus femoris muscle. The results showed similar behaviour of diffusion among the two datasets. The apparent diffusion coefficient (ADC) and fractional anisotropy (FA) values within the phantom were determined to be $2.50 \times 10^{-3} \frac{mm^2}{s}$ and 0.46, compared to $2.10 \times 10^{-3} \frac{mm^2}{s}$ and 0.45 found in muscle. Consistently, the preferred direction of diffusion in the phantom was found to follow the curvature of the strands, just as in the muscle measurement the orientation of diffusion coincides with the directionality of the muscle fibers. This study demonstrated a novel approach to phantom fabrication that accurately replicates the diffusion behaviour found in skeletal muscle.

Contents

1 Introduction **4**

2 Methods **8**

2.1 Phantom fabrication 8

2.2 MRI acquisition 11

2.3 DTI analysis 11

3 Results **12**

4 Discussion **19**

4.1 Results interpretation 19

4.2 Study limitations and future perspectives 22

5 Conclusion **23**

6 Acknowledgments **24**

7 References **24**

1 Introduction

The skeletal muscle is a hierarchical, highly organized tissue containing long contractile cells named myofibers, bundled together to form fascicles, which align to form the whole muscle structure (Figure 1) [1, 2]. These subcompartments of the skeletal muscle are densely packed in the extracellular matrix (ECM) [3]. The architecture of the muscle represents the perfect biological example of the structure-function relationship, in which both the microscopical and macroscopical structural elements are important determinants of the muscle's functional features [2, 4]. To accurately characterize the microstructure of the skeletal muscle there is a need for a non-invasive, quantitative technique that can contribute toward muscle pathology diagnosis.

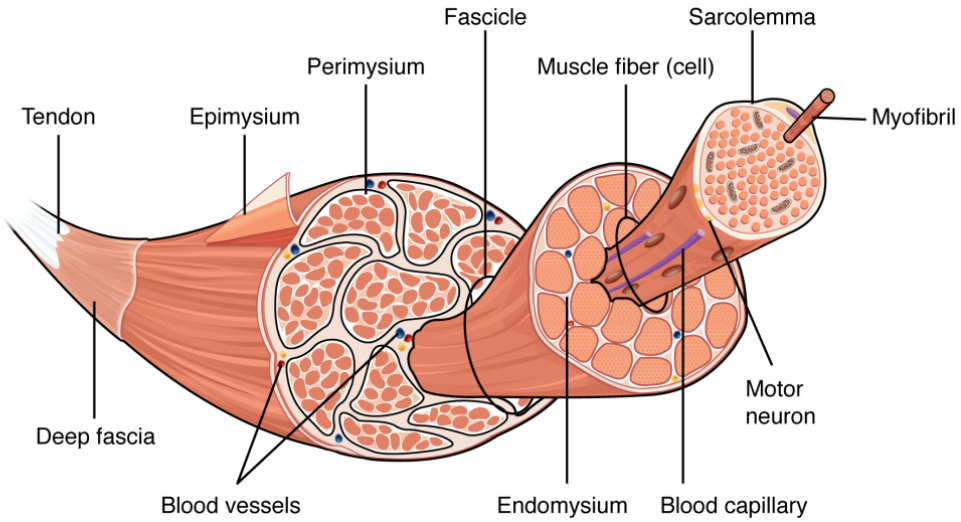

Figure 1: *Hierarchical structure of the skeletal muscle tissue [5].*

Diffusion tensor imaging (DTI) is a magnetic resonance imaging (MRI) technique that quantifies both the amount and direction of water diffusion within the human tissue [6]. DTI measures the preferential water molecule diffusion, providing qualitative and quantitative information concerning the imaged tissue. The anisotropy hindering water diffusion in a particular microstructure gives insights concerning the degree of alignment and structural integrity of cellular structures [7]. The amount of diffusion along a particular direction is calculated using the Stejskal-Tanner equation [8].

$$S_{DWI} = S_0 e^{-bD} \tag{1}$$

In equation (1), S_{DWI} represents the signal obtained with the diffusion gradients, S_0 is the signal without the diffusion gradients (normal T_2 image), b is determined by the strength, timing, and duration of the gradients, while D represents the amount of diffusion in a particular direction. Once this measurement is achieved, the covariance matrix can be defined. The diffusion matrix incorporates the diffusivity along the three spatial dimensions, using a three-dimensional Gaussian distribution that accounts for the displacement of the water molecules [9].

$$\begin{pmatrix} D_{xx} & D_{xy} & D_{xz} \\ D_{yz} & D_{yy} & D_{yz} \\ D_{zx} & D_{zy} & D_{zz} \end{pmatrix}$$

The 3x3 symmetric matrix is characterized by three orthogonal eigenvectors (ϵ_1, ϵ_2, ϵ_3) and three positive eigenvalues (λ_1, λ_2, λ_3). The eigenvectors are representative of the directions of diffusion, and the eigenvalues for the amount of diffusion corresponding to each direction, together defining the diffusion tensor (Figure 2) [10]. The major eigenvector therefore indicates the primary (preferred) direction of diffusion. In fibrous tissues, with a high degree of anisotropy, the primary eigenvector also defines the directionality of the fiber tract within the tissue. This enables tractography analysis, used as a 3D modeling technique for determining fiber orientation [11].

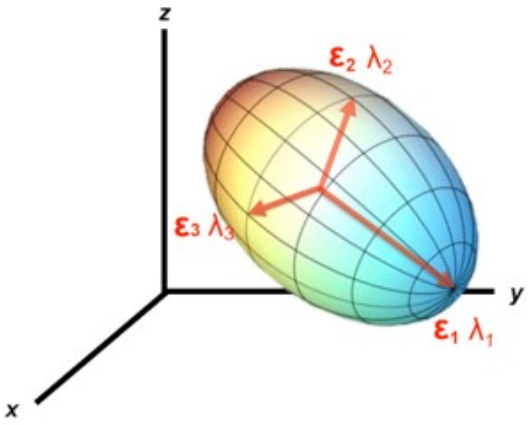

Figure 2: *Diffusion tensor composed of the three eigenvalues (λ_1, λ_2, λ_3) and three eigenvectors (ϵ_1, ϵ_2, ϵ_3); the ellipsoid shape denotes anisotropic diffusion; in this case, the major eigenvector is ϵ_1, as the corresponding eigenvalue is the highest (λ_1); therefore, the preferred direction of diffusion would be along ϵ_1. For perfect isotropic diffusion $\lambda_1 = \lambda_2 = \lambda_3$. [12]*

Knowing the characteristic eigenvectors and eigenvalues, multiple meaningful parameters can be derived. The most common parameters when performing DTI analysis are the apparent diffusion coefficient (ADC) and fractional anisotropy (FA), which provide information about the amount of diffusion, and the degree to which the diffusion is restricted, respectively. The derivation of these parameters is according to the equations (2) and (3) [13].

$$ADC = \frac{\lambda_1 + \lambda_2 + \lambda_3}{3} \tag{2}$$

$$FA = \sqrt{\frac{3}{2}} \frac{(\lambda_1 - ADC)^2 + (\lambda_2 - ADC)^2 + (\lambda_3 - ADC)^2}{\lambda_1^2 + \lambda_2^2 + \lambda_3^2} \tag{3}$$

Analyzing the structure of the skeletal muscle, the long, tightly packed muscle fibers create an anisotropic environment, favoring preferential diffusion. Furthermore, the membrane surrounding the muscle cells called sarcolemma is known to be the main factor responsible for diffusion restriction in muscle [14]. Due to this geometry, the diffusion is more restricted perpendicular to the muscle fiber, than along the muscle

cell, with literature values indicating typical diffusion coefficients of $1.3 \times 10^{-3} \frac{mm^2}{s}$ and $2.2 \times 10^{-3} \frac{mm^2}{s}$, respectively [4]. This anisotropic environment enables DTI analysis as demonstrated in previous literature [15]. The aforementioned DTI parameters are known to be sensitive to skeletal muscle changes associated with chronic diseases and injury. Conditions such as fibrosis, fiber atrophy/hypertrophy, or increased sarcolemma permeability are closely related to the diffusion behaviour within the tissue [1]. Therefore, DTI can contribute to the early detection and quantification of changes regarding muscle microstructure leading to the referred affections.

Although DTI represents a reliable tool for assessing muscle architecture, there are certain limitations of MRI acquisition that can impact the quantification of the diffusion metrics. Factors such as magnetic field inhomogeneity, RF interference, Eddy currents, and movement create artifacts that could lead to erroneous DTI quantification [16]. Thus, to ensure the reliability of the studies, there is a need for phantom validation of the DTI complex analysis techniques. Furthermore, the possibility to dictate certain parameters within a known environment would lead to a deeper understanding of the behaviour of water diffusion under set circumstances. Generally, DTI phantoms are objects designed to approximate restricted diffusion in fibrous tissue. They are validation tools that offer accurate information about the underlying microstructural features, enabling both quantitative and qualitative evaluations [17]. A few phantoms were developed to simulate the diffusion behaviour within skeletal muscle, most being designed to validate tractography analysis in brain tissue [18, 19]. Berry *et al.* conducted a study in which 3D-printed phantoms were fabricated with idealized and histology-based muscle geometry. The 3D printing technique used enabled fiber fabrication at a relevant size scale, with diameters of 30 to 70 μm [3]. However, no phantoms were designed to faithfully replicate the amount and direction of water diffusion specific to skeletal muscle tissue.

The focus of this study is to design a DTI-compatible phantom that would serve as a muscle diffusion model. The phantom would closely replicate the diffusion behaviour in the skeletal muscle and would be compared to DTI measurements from anatomical muscle tissue. It is hypothesized that the induced amount and direction of diffusion within the phantom can be identified using DTI experiments. Also, the metrics resulting from DTI measurements in the phantom should closely resemble the measurements in human muscle tissue.

2 Methods

2.1 Phantom fabrication

To replicate the curved alignment of the pennate muscles, the muscle fibers were represented by multiple arcs of circle. A single layer within the structure of the phantom consists of 21 concentric 90° arcs of circles with increasing radius (Figure 3a). Therefore, the radius of the arcs ranges from 1mm to 40mm.

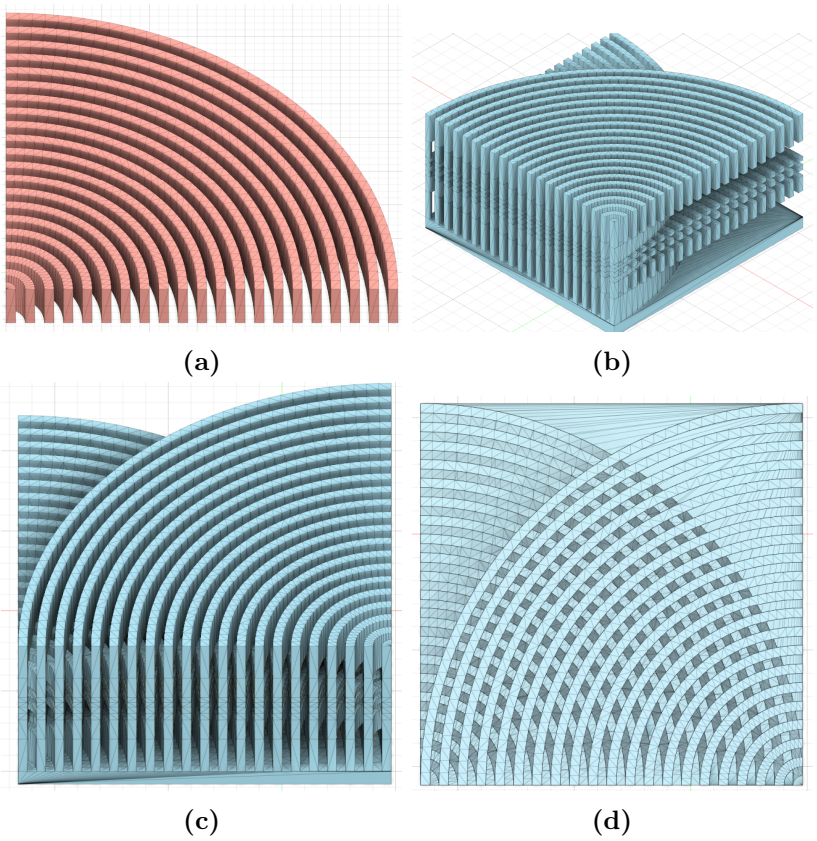

Figure 3: *Design of the structure of the phantom; (a) depicts the alignment of the 21 concentric arcs of circle with increasing radius; in (b), (c), (d) the layer from (a) is mirrored and stacked in 8 layers of different height to form the final structure.*

The final extruded layer has an arc thickness of 1mm, as well as a spacing between arcs of 1mm. The design of the layer was achieved in Autodesk Fusion 360 software [20]. Furthermore, the designed layer was mirrored and stacked together in an

alternating manner with different layer thicknesses to form the final structure (Figure 3b). By overlaying the layers in an alternating manner, an intersection pattern between the walls of each layer is formed. The layer thickness decreases towards the center of the phantom, resulting in an increased rate of intersection between the stacked layers. The assembly was performed in Autodesk Tinkercad software [21] and consisted of 8 layers of different heights. Figure 4 displays the final dimensions of the phantom.

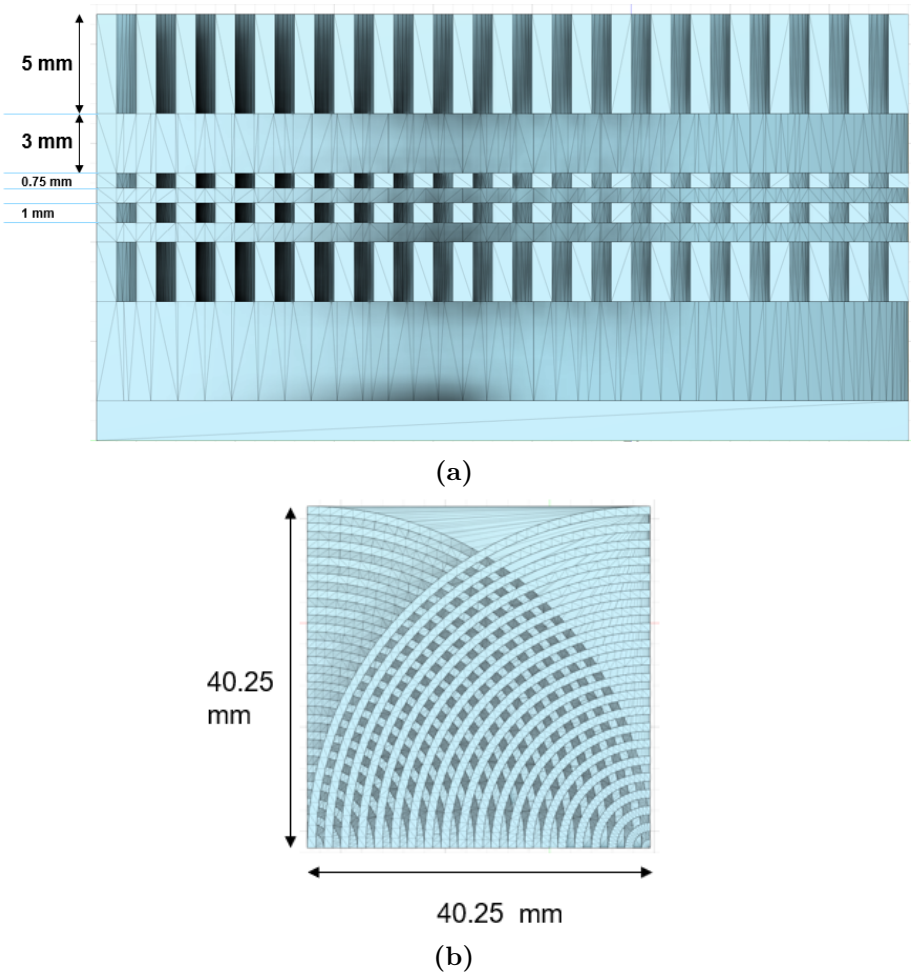

Figure 4: *Dimensions of the phantom; (a) side view of the final structure with annotations for the different layer thicknesses (the layer thickness decreases towards the center of the structure); (b) length and width of the phantom.*

After completing the design of the phantom, the structure was 3D printed using the

stereolithography (SLA) technique by a FORMLABS 3B printer using standard grey V4 resin. After printing, the structure was submerged in isopropyl alcohol solvent to eliminate excess resin, and the product was then cured using UV light.

To further replicate the structure of the skeletal muscle tissue, agar hydrogel of different concentrations was inserted between the walls of the 3D printed structure, accounting for the extracellular matrix (ECM) around the muscle fibers. The hydrogel was obtained by firstly mixing agar powder with deionized water to create three 150mL agar solutions of 0.5%, 1%, and 1.2% agar concentration. The solution was then autoclaved at $121°C$ to ensure the homogeneity and sterility of the solution. As the agar hydrogel is a temperature-sensitive hydrogel, it has a gelation point of around $35°C$ and a melting point of $85°C$ [22]. After autoclaving, when cooled down below the gelation point, the water molecules serve as the glue that binds the agar polymers together, resulting in a highly porous cross-linked hydrogel (Figure 5)[23]. To ensure the even spread of hydrogel within the 3D printed structure, the three agar hydrogels were reheated in a water bath at $90°C$ overnight for even liquefying. The solutions were then poured at a time in a vessel containing the phantom to create three homogeneous layers of hydrogel of different agar concentrations. The result was a step gradient of agar concentration throughout the hydrogel within the phantom.

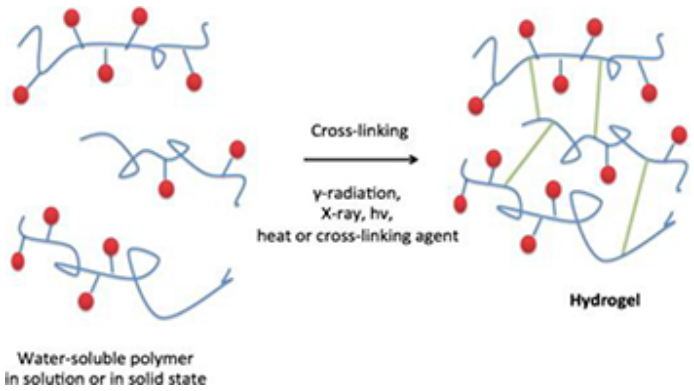

Figure 5: *Cross-linking process of agar hydrogel; The agar powder composed of agar polymers is dissolved in water, the temperature acting as a cross-linking agent between agar polymers and water molecules; the final hydrogel contains both free and trapped water, the former one being able to freely diffuse through the hydrogel structure.*

2.2 MRI acquisition

The DTI scanning was carried out with a 3T Siemens Prisma scanner. There were two scanning sessions for both phantom and human experiments. One participant was recruited to assess DTI measurements in human muscle tissue. The 22 years old, male volunteer had no history of muscle-related injury or pathology. Both a DTI and an anatomical scan were performed on the upper leg muscles. The acquisition parameters for both phantom and human scans are presented in Table 1.

Acquisition parameters	Phantom scan	Muscle scan
Scanner	Siemens Prisma (3T)	Siemens Prisma (3T)
Coil type	64 channel head coil	18 channel body coil
Scan localization	phantom	upper leg muscle
Orientation	coronal	axial
b-values	0/50/100/200/400	0/50/100/200/400/ 800/1000
Number of diffusion encoding directions	6	6
TE/TR (ms)	68/4060	57/3000
Slice thickness (mm)	1.1	3
Voxel size (mm)	$1.1 \times 1.1 \times 1.1$	$1.1 \times 1.1 \times 3$
Number of slices	30	30

Table 1: *DTI acquisition parameters for both muscle and phantom scans.*

2.3 DTI analysis

The acquired DTI data was first pre-processed to eliminate possible artifacts and to convert the data into the desired format. Therefore, the DICOM files were converted into NIfTI format using dicom2niix software [24]. The resulting data was corrected for eddy currents using FSL software [25], the phantom data being also smoothened with 1mm Full Width at Half Maximum (FWHM) using SPM12 software [26]. Furthermore, the pre-processed data was introduced in the DTIFIT module of FSL, which fits the diffusion tensor model to obtain scalar DTI maps (ADC, FA), and preferred diffusion orientation. The orientation of the fibers are approximated by

calculation of the diffusion eigenvectors and eigenvalues, which indicate the primary direction and amount of diffusion, respectively. The phantom data was also subjected to tractography analysis using TrackVis software to determine the resulting fiber orientation [27].

After completing data processing, the first point of analysis consisted of assessing the influence of hydrogel stiffness (agar concentration) on the amount of diffusion, as well as on the degree of diffusion restriction, within the hydrogel alone. Therefore, multiple regions of interest (ROIs) were set in the phantom ADC and FA map for each layer corresponding to a fixed concentration of agar. The average voxel value within the set ROIs was used to compare the ADC and FA values for the three different agar concentrations. Furthermore, the same procedure was used to determine the ADC and FA values within the structural part of the phantom (within the 3D printed structure) and within the rectus femoris muscle, which was identified using the anatomical scans. This was achieved by selecting ROIs in a central area of the phantom and in the rectus femoris muscle. Additionally, the diffusion eigenvectors and eigenvalues maps were extracted for phantom and muscle measurements. Using MATLAB, the x, y, and z components of the major eigenvector were extracted and compared for both the phantom and muscle measurements, leading to the evaluation of the preferred direction of diffusion within specified ROIs. The primary eigenvector map was also qualitatively assessed by visually checking if the orientation of the vectors within voxels corresponds to the orientation of the fiber tracts.

3 Results

Incorporating the 3D printed structure (Figure 6a) and the three layers of 0.5%, 1%, and 1.2% agar concentration, the final phantom was successfully fabricated (Figure 6c).

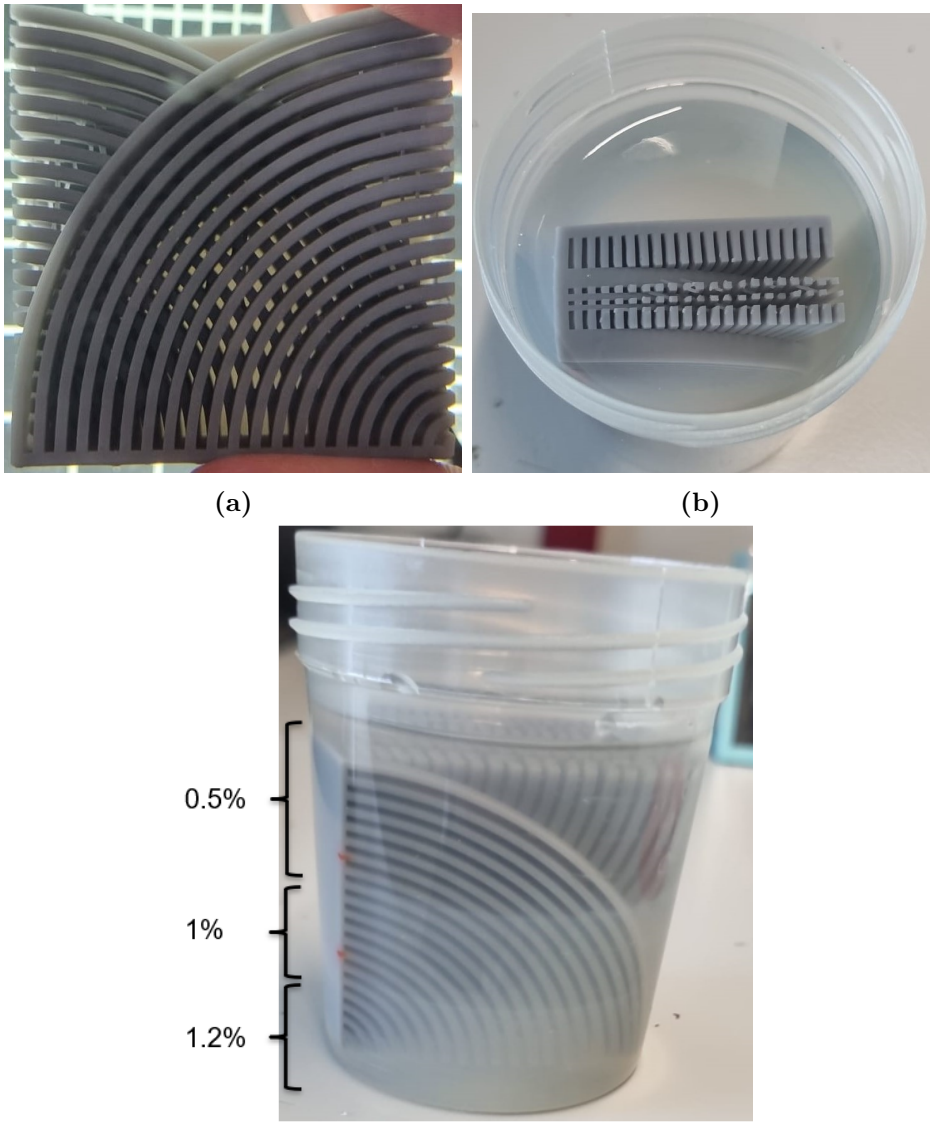

Figure 6: *(a) 3D printed structure fabricated using SLA printing; (b), (c) final phantom composed of the 3D structure immersed in three layers of different hydrogel concentration.*

Furthermore, the DTI scan of the phantom is presented in Figure 7, in axial (7a), coronal (7b), and sagittal plane (7c).

The isolation of the rectus femoris muscle for DTI analysis was possible by masking the region identified on the anatomical leg scan, as seen in Figure 8.

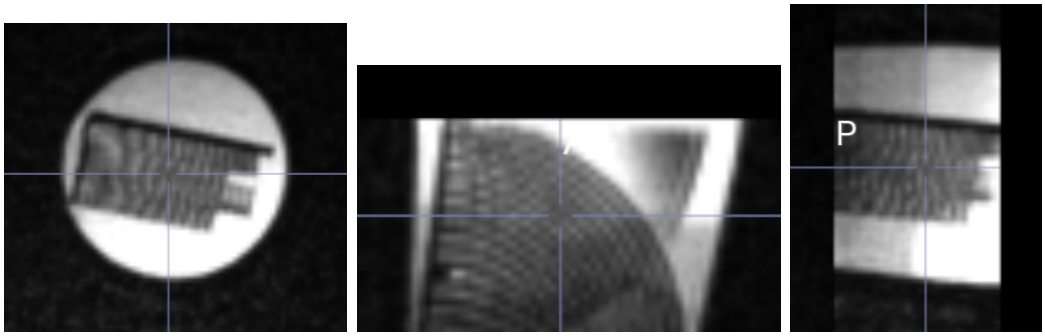

(a) **(b)** **(c)**

Figure 7: *Smoothened and eddy-corrected DTI scans of the phantom in axial, coronal, and sagittal planes, respectively.*

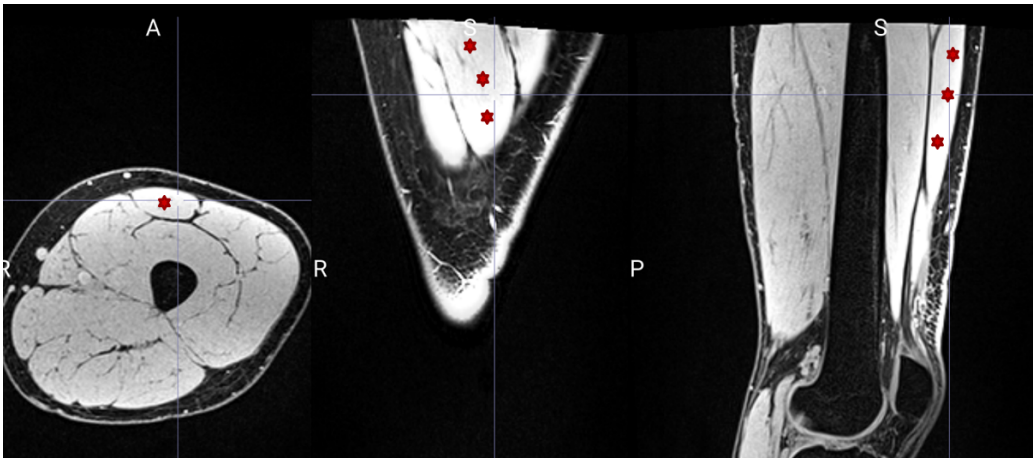

Figure 8: *Anatomical scan of the upper leg muscles obtained using Dixon acquisition method [28]. The red stars indicate the position of the rectus femoris muscle within the image.*

Once the DTI metrics were extracted, the average ADC and FA values were computed for each of the plain hydrogel layers. The results are visible in Table 2. No correlation between the stiffness of the hydrogel (which is proportional to the agar concentration) and the amount of diffusion could be identified at first glance. The disproportionality can be also observed when analyzing the degree of diffusion restriction (FA value).

Agar concentration (%)	ADC value ($\times 10^{-3} \frac{mm^2}{s}$) / STD	FA value / STD
1.2	2.28 / 0.24	0.29 / 0.07
1	2.12 / 0.19	0.23 / 0.08
0.5	2.40 / 0.14	0.31 / 0.10

Table 2: *Table containing apparent diffusion coefficient and fractional anisotropy values for pure hydrogel (without 3D printed structure); The regions of interest were set on each of the three hydrogel layers of different concentrations of agar. The values within the ROIs were averaged for each layer to obtain the final ADC and FA values. The standard deviation of each measurement was also incorporated in the table.*

The same DTI parameters were then assessed concerning the rectus femoris muscle and the structured part of the phantom. Both ADC and FA maps were masked to only extract average values within the rectus femoris muscle and central area of the phantom. Table 3 shows the correlation between the amount of diffusion found in both phantom and muscle. The similarity becomes even bigger when analyzing the fractional anisotropy values.

DTI parameters	Phantom	Muscle
ADC value ($\times 10^{-3} \frac{mm^2}{s}$) / STD	2.50 / 0.18	2.10 / 0.27
FA value / STD	0.46 / 0.10	0.45 / 0.12

Table 3: *Table containing apparent diffusion coefficient and fractional anisotropy values for both the structured part of the phantom and rectus femoris muscle; The regions of interest were set in the center of the phantom, as well as in the center of the muscle. The average and standard deviation of the values within the ROIs were computed for the ADC and FA maps corresponding to both phantom and muscle datasets.*

Moreover, the preferred direction of diffusion within muscle and phantom was assessed from multiple standpoints. First, Figure 9a displays the major diffusion eigenvector map of the muscle measurements on top of the ADC map. At each voxel, the intensity is dictated by the ADC value, while the color-coded vectors represent the direction of the primary eigenvector. Although not visible in the axial slice (rightmost image), in the coronal and sagittal views of the rectus femoris muscle, the orientation of the eigenvector points along the fiber muscle tracts. Blue color, which is predominantly seen in Figure 9a signifies in-plane diffusion with respect to the axial view, which is again parallel to the muscle fiber bundles. The amount of diffusion along the orientation of the presented eigenvector was also extracted, yielding

$3.18 \times 10^{-3} \frac{mm^2}{s}$, which is considerably larger than the mean ADC of $2.10 \times 10^{-3} \frac{mm^2}{s}$, specific for all encoding directions of diffusion. The diffusion tensor orientation in Figure 9b follows the same direction as the major eigenvector, diffusion appearing to be predominantly in z-direction (blue color), representing in-plane orientation, perpendicular to the axial view.

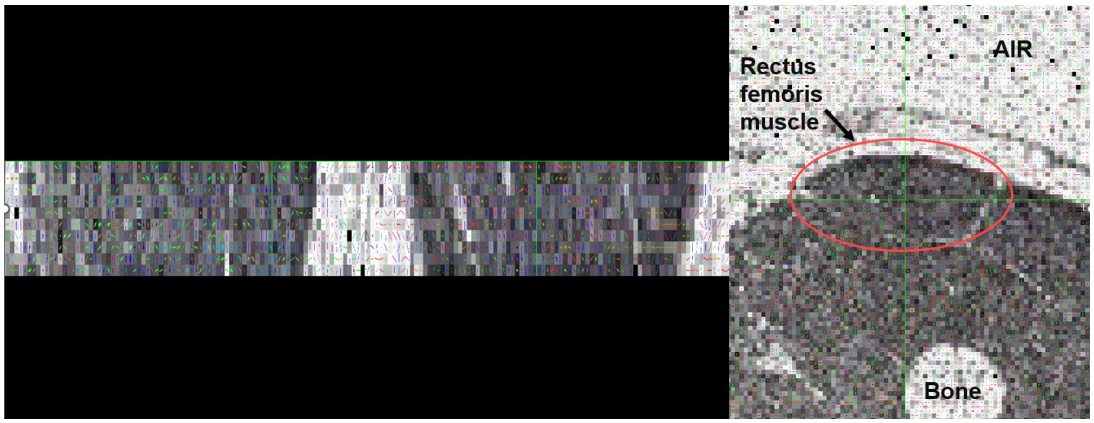

(a)

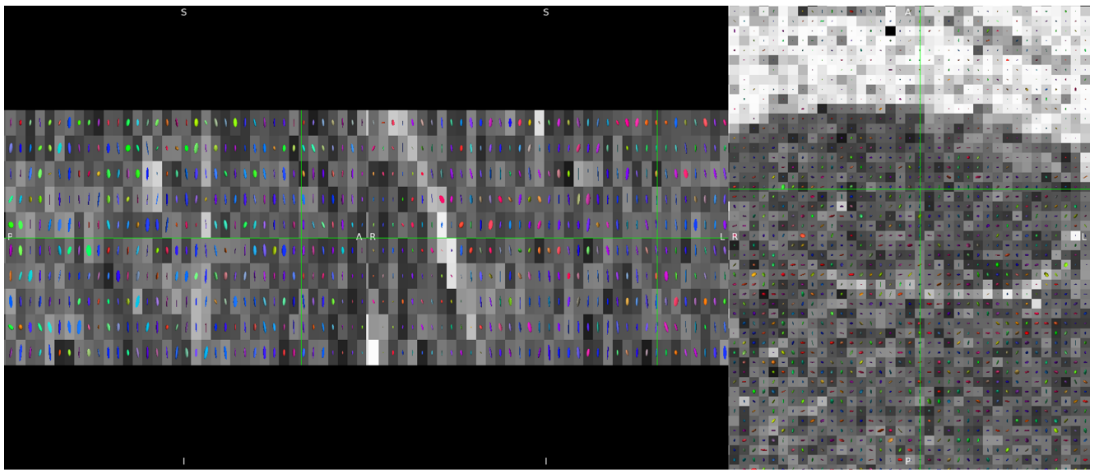

(b)

Figure 9: *Major eigenvector map (a) and diffusion tensor map (b) of the rectus femoris muscle in the sagittal, coronal, and axial plane, from left to right. The red, green and yellow vectors(a)/tensors(b) within each voxel are color-coded to display the direction of the primary eigenvector/tensor, which indicates the preferred direction of diffusion; the color red represents vector/tensor orientation in the axis (left-right), green color represents vector/tensor orientation in y-axis (up-down), and blue color represents vector/tensor orientation in z-axis (in-plane).*

To quantify the primary direction of diffusion in muscle, the x, y, and z components (corresponding to the three encoding colors red, green, and blue) of the major eigenvector (Figure 9a) were extracted at each voxel within the rectus femoris muscle and plotted in a histogram (Figure 10). Within the analyzed voxels, the major eigenvector component corresponding to the z orientation appears larger than the other two components. Therefore, it can be observed that the z component is dominant in dictating the preferred eigenvector orientation. Furthermore, the separate x, y, and z components were summed, with x components adding to -71.90, y components to -29.54, and z components to 160.74. The magnitude of the summed components pointing in z-direction is significantly higher than the other two axes.

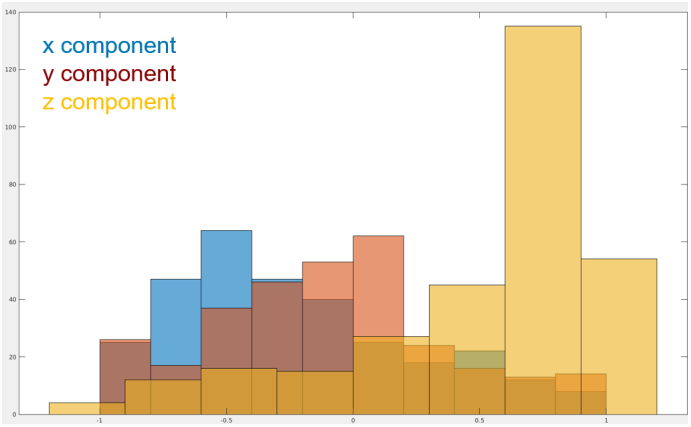

Figure 10: *Histogram representing the count of the individual x, y, and z components of each vector within the primary eigenvector map of the rectus femoris; yellow represents the count of z components, red, the count of y components, and blue, the count of x components.*

The same line of analysis was followed in investigating the preferred direction of diffusion in the phantom. As visible in Figure 11, both the tensor (Figure 11c) and the major eigenvector (Figure 11b) orientation are in line with the curvature of the walls of the phantom. The amount of direction corresponding to this orientation is also larger compared to the mean ADC of the phantom ($3.80 \times 10^{-3} \frac{mm^2}{s}$ compared to $2.5 \times 10^{-3} \frac{mm^2}{s}$), suggesting more diffusion along the curvature of the strands than in other directions. Although visually, the eigenvectors and the tensors appear to be primarily along the x-axis (red color), the histogram in Figure 12 of x, y, and z components of the eigenvector does not show a clear predominance.

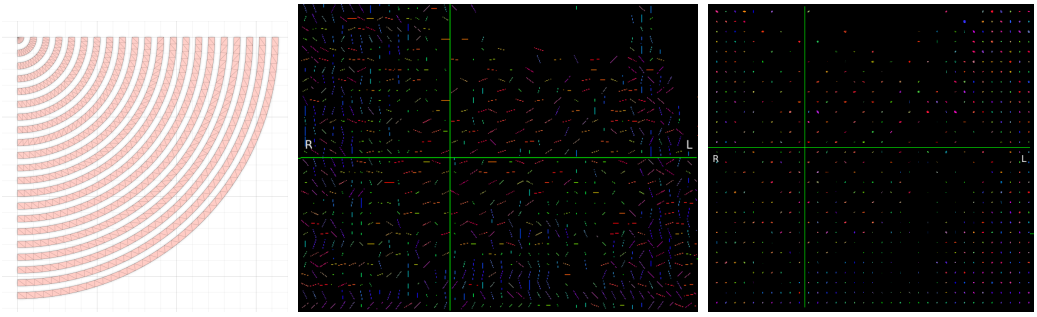

(a) **(b)** **(c)**

Figure 11: *(a) top view of the orientation of one of the layers within the 3D printed structure; (b) major eigenvector map of the phantom; (c) diffusion tensor map of the phantom. The color code represents the different orientations of the vectors/tensors; red represents direction along the x-axis (left-right), green represents direction along the y-axis (up-down), and blue represents direction along the z-axis (in-plane).*

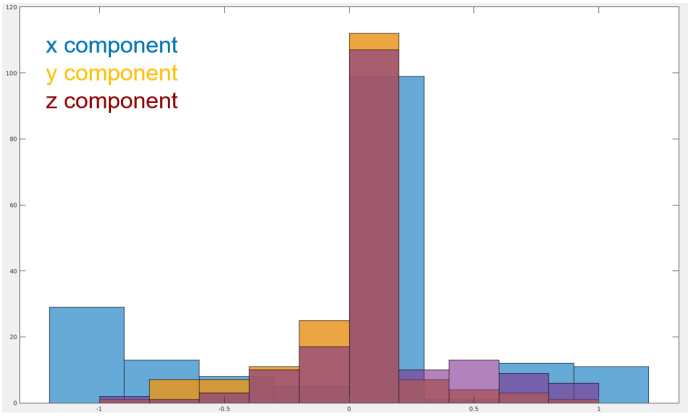

Figure 12: *Histogram representing the count of the individual x, y, and z components of each vector within the primary eigenvector map of the phantom; yellow represents the count of y components, red, the count of z components, and blue, the count of x components.*

Finally, Figure 13 illustrates the result of the tractography analysis carried out on the phantom. The tractography result was expected to closely replicate the location and directionality of the different layers of curved walls within the phantom. However, the simulated tracts did not coincide with the expected orientation, thus the original structure of the phantom could not be observed within the reconstructed fibers.

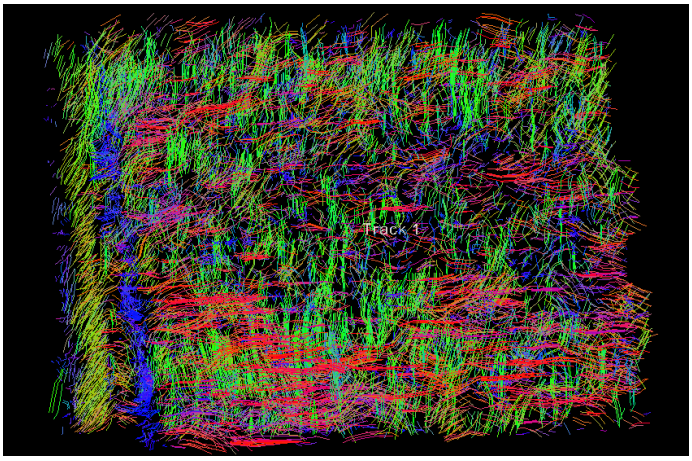

Figure 13: *Result of the tractography analysis on the phantom measurements; The fibers were reconstructed based on the preferred direction of diffusion and the diffusion restriction imposed by walls of the phantom.*

4 Discussion

4.1 Results interpretation

The goal of this study was to develop a DTI-compatible phantom that would replicate the diffusion behaviour within skeletal muscle tissue. The study demonstrated a technique that can be employed to fabricate phantoms that control the characteristics of diffusion, such that the hallmarks of water diffusion in muscle are closely reproduced. Accounting for both the cellular and extracellular domains of the muscle tissue, the developed phantom incorporates two components, simulating both the muscle fiber structure and the extracellular matrix in between. The aim of the two components of the phantom was to influence the two main features of diffusion: amount and direction. Therefore, the 3D-printed structure was designed to determine a preferential direction of diffusion, and the different concentrations of hydrogel were introduced to influence the amount of diffusion within the phantom. Although not anatomically relevant for the muscle organization, the structure of the 3D printed piece was created to account for the intersection between strands. Thus, the thickness of the stacked layers decreases towards the center of the phantom, as seen in Figure 4a, leading to an increased rate of intersection between the alternated mirrored layers. As the slice thickness used in the MRI acquisition parameters is around 1mm and the smallest layer thickness is 0.75mm, the phantom enables

analysis of the orientation of the crossing strands below the resolution of the scan. Another feature of the phantom is that the overlay of the mirrored layers forms a gradient of increasing angles of intersection between the strands, as seen in Figure 4b. Therefore, the angles of intersection range from almost 0° at the bottom of the structure to over 90° at the top. This allows for investigation concerning the resolution of distinguishing between two different directions of diffusion at the location where two strands intersect. The reason for performing this analysis is that at small angles of intersection, the two different directions of diffusion corresponding to the two intersecting fibers are not distinguished anymore.

The first point of analysis consisted of assessing the influence of agar concentration in the pure hydrogel on the apparent diffusion coefficient and fractional anisotropy values. As the ratio of bound to free water in the hydrogel depends on the amount of polymer introduced, it was hypothesized that the amount of diffusion would linearly decrease with increasing agar concentration. However, Table 2 shows no correlation that would support the stated hypothesis. Although the largest ADC value is found for the lowest concentration of agar (0.5%) as expected, the trend is not followed by the increasing concentrations of agar. Analyzing the degree of diffusion restriction, the observed FA values were larger than expected. An FA value of 0 represents pure isotropic diffusion and 1 represents pure anisotropic diffusion. The calculated FA values indicate the presence of a preferred direction of diffusion in the plain hydrogel. As the structure of the hydrogel is characterized by random cross-links created by the agar polymers and water molecules, it was not expected that the water would diffuse along a preferred direction. The hydrogel was supposed to incorporate no structural orientation that would allow free water diffusion along a specific direction. Therefore, FA values for plain hydrogel were anticipated to be close to 0, denoting isotropic diffusion, regardless of the agar concentration. However, the expectations were not valid, as the FA values range between 0.23 and 0.31. Also, no dependency between agar concentration and diffusion restriction could be identified. This lack of correlation between agar concentrations and DTI metrics might be due to the small sample size of agar concentrations. A concentration gradient with a larger range of concentrations might indicate results closer to the proposed hypothesis.

The designed phantom was compared with the measurements in human skeletal muscle to validate the diffusion quantification achieved on the phantom data. Therefore, Table 3 presents the ADC and FA values found in the phantom to be very similar to

the values extracted from the rectus femoris muscle measurements. The values for the rectus femoris muscle found in this study were also compared to other literature results for ADC and FA in skeletal leg muscle [29, 30, 31, 32, 33, 34]. In the studies conducted by Li *et al.* and Longwei *et al.*, the ADC values for the rectus femoris muscle for healthy controls were found to be $1.02 \times 10^{-3} \frac{mm^2}{s}$ and $0.92 \times 10^{-3} \frac{mm^2}{s}$, respectively [31, 30]. Nonetheless, other publications suggest higher ADC values for the upper thigh muscles ($1.80 \times 10^{-3} \frac{mm^2}{s}$ [33]; $1.74 \times 10^{-3} \frac{mm^2}{s}$ [31]). The amount of diffusion of $2.10 \times 10^{-3} \frac{mm^2}{s}$ found in this study is higher than the average results found in other studies. However, literature values are prone to high inter-subject and inter-scanner variability due to different acquisition parameters (different b-values, number of averages, number of diffusion encoding directions), which explains the difference in obtained values. The discrepancy with literature values can be observed also regarding the FA-obtained values. Previous studies indicate values of 0.24-0.29 for rectus femoris muscle, while this study reports a fractional anisotropy of 0.45 [30, 31, 33]. Although there is a high variability between the literature and this study concerning muscle measurements, the similarity between the developed phantom and muscle quantification, suggests successful replication within the phantom of the water diffusion behaviour in skeletal muscle.

The comparison between phantom and muscle measurements was also assessed by analyzing the preferred direction of diffusion within both environments. Therefore, Figure 9a and Figure 11b display the orientation of the major diffusion eigenvector (for both phantom and rectus femoris muscle), which coincides with the preferred direction of diffusion within the two structures. From a qualitative standpoint, the orientation of the primary eigenvector appears to follow the direction of the fibers present in both phantom and muscle. Therefore, the eigenvector corresponding to the muscle is oriented primarily along the z-axis (blue color-coded), which also indicates the directionality of the muscle fibers. The same diffusion behaviour is observed in the phantom, where the direction of the eigenvector points along the curvature of the tracts within the phantom. To support this result, the tensor map was also displayed for both phantom and muscle (Figure 11c; Figure 9b), showing the same orientation specific to the direction of the fiber tracts in both cases. As both the major eigenvector and diffusion tensor are indicative of the primary direction of diffusion, it can be concluded that the 3D printed structure determined a diffusion restriction similar to the one found in human skeletal muscle. In both cases, the structural environment induced the directionality of diffusion along the orientation of the fibers/walls. Furthermore, from a quantitative standpoint, the components

of the major eigenvector along the x, y, and z axis were extracted for phantom and human measurements (Figure 12; Figure 10). Concerning the muscle analysis, the z component of the eigenvector was clearly dominant in comparison to the other two axes, confirming again the preferred diffusion along the muscle fiber. On the other hand, the quantification of the different components of the eigenvector corresponding to the diffusion direction in the phantom is almost equal among the x, y, and z axes. The orientation of the curved walls within the phantom is not purely in the x, y, or z direction, making the quantification of these components more difficult to assess.

The tractography analysis of the phantom was inconclusive, as the orientation of the reconstructed fibers did not correlate with the structure of the phantom (Figure 13). No preferred direction of diffusion was identified along the curvature of the phantom tracts, in contrast to the tensor and major eigenvector directionality. This unsatisfying result might be the outcome of poor setting of the MRI acquisition parameters. A recent study recommends that the number of diffusion encoding directions for meaningful tractography analysis to be a minimum of 18 directions, while the acquisition parameters used in this study include just 6 directions [35]. The choice of parameters most likely had a negative impact on the tractography reconstruction, as insufficient data regarding the direction of diffusion was available.

4.2 Study limitations and future perspectives

There are several limitations concerning the design and development of the phantom and the analysis of the acquired data. First, the overall size of the phantom and the spacing between the curved walls were too large to faithfully replicate the structure and fiber organization of the muscle tissue. The diameter of the muscle fibers ranges from 10 to 100μm, the spacing between the fibers being 3 to 5μm [36, 1]. As the resolution of the 3D printing technique used was 0.2 mm, the relevant size scale could not be achieved. For future iterations, a 3D printing method with a much higher resolution is recommended for accurately replicating the micro-architecture of the skeletal muscle. However, if the distancing between the walls of the phantom is drastically decreased, the inserted hydrogel might have problems diffusing evenly throughout the structure of the phantom. Therefore, a compromise is required to maintain both the decreased spacing and the presence of the hydrogel.

Secondly, a high degree of structural orientation was observed in plain hydrogel measurements. Although the architecture of the hydrogel is supposed to be defined by random cross-links of the agar polymers, the results showed a preferred direction of diffusion, as the FA values were larger than expected for plain hydrogel. Therefore, when pouring the hydrogel into the vessel containing the 3D-printed structure, a certain structural orientation might have been induced. For accurate analysis of the direction of diffusion, the diffusion within the hydrogel needs to be as close to isotropic. In this way, just the orientation of the inserted structure will dictate the preferred direction of diffusion.

Additionally, the MRI acquisition parameters were not ideal for the intended analysis. The tractography result on the phantom measurements was inconclusive mainly due to the reduced number of diffusion encoding directions used at acquisition. For future iterations, a number of at least 18 diffusion directions are suggested for accurate tractography analysis. Due to time restriction, the analysis regarding the crossing fibers of the phantom could not be carried out. Another future perspective consists of the assessment of the diffusion direction as a function of the intersection angle between the crossing strands.

5 Conclusion

The study presented a methodology of successfully replicating the diffusion behaviour in human skeletal muscle using a phantom. The two components of the phantom achieved their goal of influencing water diffusion, simulating the structure of the skeletal muscle. Thus, different amounts of diffusion were induced within the phantom using different agar concentrations in hydrogels. Moreover, directionality was introduced in free water diffusion using a 3D-printed structure with alternating wall orientation. The results obtained within this study might lead to a better understanding of the characteristics of water diffusion and how that can be influenced towards anatomically relevant problems.

6 Acknowledgments

The author would like to express his sincere gratitude towards the two supervisors of this bachelor project (Dr. Remco Renken and Dr. Prashant Sharma) for their guidance and support towards the completion of this project.

Additionally, the stereolithography-based 3D printing method was supported by the University Medical Center Groningen Instrumental Research Facility 'Instrumentmakerij'. The author would like to thank Hans Thole for his help in fabricating the 3D-printed structure.

7 References

References

[1] David B Berry, Benjamin Regner, Vitaly Galinsky, Samuel R Ward, and Lawrence R Frank. Relationships between tissue microstructure and the diffusion tensor in simulated skeletal muscle. *Magnetic resonance in medicine*, 80(1):317–329, 2018.

[2] Richard L Lieber. *Skeletal muscle structure, function, and plasticity*. Lippincott Williams & Wilkins, 2002.

[3] David B Berry, Shangting You, John Warner, Lawrence R Frank, Shaochen Chen, and Samuel R Ward. A 3d tissue-printing approach for validation of diffusion tensor imaging in skeletal muscle. *Tissue Engineering Part A*, 23(17-18):980–988, 2017.

[4] Anneriet M Heemskerk and Bruce M Damon. Diffusion tensor mri assessment of skeletal muscle architecture. *Current Medical Imaging*, 3(3):152–160, 2007.

[5] Transparent Tissue Clipart . https://www.pngitem.com/middle/hhxTibh$_t ransparent-tissue-clipart-muscle-structure-hierarchy-hd-png/$.

[6] Adam Kirton. Modeling developmental plasticity after perinatal stroke: defining central therapeutic targets in cerebral palsy. *Pediatric neurology*, 48(2):81–94, 2013.

[7] Ahmed Abdel Khalek Abdel Razek, Manar Mansour, Elsharawy Kamal, and Suresh K Mukherji. Mr imaging of oral cavity and oropharyngeal cancer. *Magnetic Resonance Imaging Clinics*, 30(1):35–51, 2022.

[8] Edward O Stejskal and John E Tanner. Spin diffusion measurements: spin echoes in the presence of a time-dependent field gradient. *The journal of chemical physics*, 42(1):288–292, 1965.

[9] Lauren J O'Donnell and Carl-Fredrik Westin. An introduction to diffusion tensor image analysis. *Neurosurgery Clinics*, 22(2):185–196, 2011.

[10] Joshua S Shimony, Robert C McKinstry, Erbil Akbudak, Joseph A Aronovitz, Abraham Z Snyder, Nicolas F Lori, Thomas S Cull, and Thomas E Conturo. Quantitative diffusion-tensor anisotropy brain mr imaging: normative human data and anatomic analysis. *Radiology*, 212(3):770–784, 1999.

[11] Timothy EJ Behrens, Stamatios N Sotiropoulos, and Saad Jbabdi. Mr diffusion tractography. In *Diffusion MRI*, pages 429–451. Elsevier, 2014.

[12] Diffusion Tensor. https://mriquestions.com/diffusion-tensor.html.

[13] Denis Le Bihan, Jean-François Mangin, Cyril Poupon, Chris A Clark, Sabina Pappata, Nicolas Molko, and Hughes Chabriat. Diffusion tensor imaging: concepts and applications. *Journal of Magnetic Resonance Imaging: An Official Journal of the International Society for Magnetic Resonance in Medicine*, 13(4):534–546, 2001.

[14] Hena R Ramay and Marko Vendelin. Diffusion restrictions surrounding mitochondria: a mathematical model of heart muscle fibers. *Biophysical journal*, 97(2):443–452, 2009.

[15] Jos Oudeman, Aart J Nederveen, Gustav J Strijkers, Mario Maas, Peter R Luijten, and Martijn Froeling. Techniques and applications of skeletal muscle diffusion tensor imaging: a review. *Journal of Magnetic Resonance Imaging*, 43(4):773–788, 2016.

[16] Denis Le Bihan, Cyril Poupon, Alexis Amadon, and Franck Lethimonnier. Artifacts and pitfalls in diffusion mri. *Journal of Magnetic Resonance Imaging: An Official Journal of the International Society for Magnetic Resonance in Medicine*, 24(3):478–488, 2006.

[17] Ivana Drobnjak, Peter Neher, Cyril Poupon, and Tabinda Sarwar. Physical and digital phantoms for validating tractography and assessing artifacts. *Neuroimage*, 245:118704, 2021.

[18] Q Ye Allen, Penny L Hubbard Cristinacce, Feng-Lei Zhou, Ziying Yin, Geoff JM Parker, and Richard L Magin. Diffusion tensor mri phantom exhibits anomalous diffusion. In *2014 36th Annual International Conference of the IEEE Engineering in Medicine and Biology Society*, pages 746–749. IEEE, 2014.

[19] Edna Marina de Souza, Eduardo Tavares Costa, and Gabriela Castellano. Phantoms for diffusion-weighted imaging and diffusion tensor imaging quality control: a review and new perspectives. *Research on Biomedical Engineering*, 33:156–165, 2017.

[20] Autodesk Fusion 360. https://www.autodesk.com/products/fusion-360/.

[21] Autodesk Tinkercad. https://www.tinkercad.com/.

[22] Shilpi Boral, Anita Saxena, and HB Bohidar. Syneresis in agar hydrogels. *International journal of biological macromolecules*, 46(2):232–236, 2010.

[23] Eliane P van Dam, Hongbo Yuan, Paul HJ Kouwer, and Huib J Bakker. Structure and dynamics of a temperature-sensitive hydrogel. *The Journal of Physical Chemistry B*, 125(29):8219–8224, 2021.

[24] Xiangrui Li, Paul S Morgan, John Ashburner, Jolinda Smith, and Christopher Rorden. The first step for neuroimaging data analysis: Dicom to nifti conversion. *Journal of neuroscience methods*, 264:47–56, 2016.

[25] Mark W Woolrich, Saad Jbabdi, Brian Patenaude, Michael Chappell, Salima Makni, Timothy Behrens, Christian Beckmann, Mark Jenkinson, and Stephen M Smith. Bayesian analysis of neuroimaging data in fsl. *Neuroimage*, 45(1):S173–S186, 2009.

[26] Statistical Parametric Mapping. https://www.fil.ion.ucl.ac.uk/spm/.

[27] TrackVis. https://trackvis.org/.

[28] Patrick Omoumi. The dixon method in musculoskeletal mri: from fat-sensitive to fat-specific imaging. *Skeletal Radiology*, 51(7):1365–1369, 2022.

[29] Osamu Yanagisawa, Daisuke Shimao, Katsuya Maruyama, Matthew Nielsen, Takeo Irie, and Mamoru Niitsu. Diffusion-weighted magnetic resonance imaging of human skeletal muscles: gender-, age-and muscle-related differences in apparent diffusion coefficient. *Magnetic resonance imaging*, 27(1):69–78, 2009.

[30] Xu Longwei. Clinical application of diffusion tensor magnetic resonance imaging in skeletal muscle. *Muscles, ligaments and tendons journal*, 2(1):19, 2012.

[31] Gui Dian Li, Ying Yin Liang, Ping Xu, Jian Ling, and Ying Ming Chen. Diffusion-tensor imaging of thigh muscles in duchenne muscular dystrophy: correlation of apparent diffusion coefficient and fractional anisotropy values with fatty infiltration. *American Journal of Roentgenology*, 206(4):867–870, 2016.

[32] Alexey Surov, Lisa Paul, Hans Jonas Meyer, Stefan Schob, Cornelius Engelmann, and Andreas Wienke. Apparent diffusion coefficient is a novel imaging biomarker of myopathic changes in liver cirrhosis. *Journal of clinical medicine*, 7(10):359, 2018.

[33] Erwan Kermarrec, Jean-François Budzik, Chadi Khalil, Vianney Le Thuc, Caroline Hancart-Destee, and Anne Cotten. In vivo diffusion tensor imaging and tractography of human thigh muscles in healthy subjects. *American Journal of Roentgenology*, 195(5):W352–W356, 2010.

[34] Li Zhang, Yanjing Zhang, Wanzhen Yao, Jing Zhou, Hailong LIU, and Jianping DING. The value of diffusion tensor imaging in the quantitative study of thigh muscles in amateur marathon runners. *Chinese Journal of Radiology*, pages 818–823, 2019.

[35] Venla Kumpulainen, Harri Merisaari, Anni Copeland, Eero Silver, Elmo P Pulli, John D Lewis, Ekaterina Saukko, Jani Saunavaara, Linnea Karlsson, Hasse Karlsson, et al. Effect of number of diffusion-encoding directions in diffusion metrics of 5-year-olds using tract-based spatial statistical analysis. *European Journal of Neuroscience*, 56(6):4843–4868, 2022.

[36] Christopher McCuller, Rishita Jessu, and Avery L Callahan. Physiology, skeletal muscle. In *StatPearls [Internet]*. StatPearls Publishing, 2023.